Numerical evolution of the center of mass and angular momentum for binary black holes

Emmanuel A. Tassone⬤,[*] Paula A. Mandrilli, Carlos N. Kozameh, Gonzalo D. Quiroga⬤, and José I. Nieva

FaMAF, Universidad Nacional de Córdoba, 5000 Córdoba, Argentina

The asymptotic approach derived by Kozameh-Quiroga provides a modern framework to obtain the evolution of global variables of isolated sources of gravitational radiation. We test the Kozameh-Quiroga formalism evolving the equations of motion for the center of mass, the intrinsic angular momentum, and several other global variables, for black hole binary coalescence. First, we evolve the equations of motion using 777 simulations from the RIT catalog of numerical data of ψ_4 [J. Healy and C. O. Lousto, Third RIT binary black hole simulations catalog, Phys. Rev. D **102**, 104018 (2020).]. We then analyze the trajectory of the center of mass and compute the final state of other physical variables after the coalescence has taken place. Finally, we show that the results obtained from our equations of motion are consistent with those in the Rochester metadata.

I. INTRODUCTION

The equations of motion for global variables describing isolated sources of gravitational radiation is an old and important area of research in general relativity (GR). Out from the many formulations presented in the literature, those using the mathematical formulation of asymptotic flatness offer the possibility of matching its predictions with observations.

The notions of Bondi mass, linear momentum, dipole mass moment, and angular momentum resemble their Minkowskian counterparts in classical field theory, except that in this case they are not conserved quantities but obey evolution equations that are derived from the field equations of GR. Linking those quantities with equations of motion for the center of mass and intrinsic angular momentum is the goal of the different approaches given in the literature [1–5].

Many of the key ideas to define and evolve those variables were presented and developed by E. T. Newman and collaborators [6,7]. More recently, these results were generalized and a relativistic approach is now available in the literature [8].

Since binary coalescence offers an excellent scenario to test predictions both in terms of numerical solutions, semianalytical approaches, and direct observations of gravitational radiation. The purpose of this work is to numerically evolve the equations of motion for the center of mass and intrinsic angular momentum for some 800 cases that were taken from the Rochester repository [9].

The main idea in this work is to present the equations, give technical details of the numerical setup and show some results both for particular cases and for the whole numerical evolutions.

To classify the binary system type, we follow the conventions of the Rochester repository, dividing the numerical outcomes in different classes according to the relative masses into equal or nonequal masses (EM or NEM). Likewise, the spins of the black holes are taken into account and we can distinguish them between nonspinning (NS), aligned (A) which are aligned with the orbital angular momentum (A) or precessing spins (P).

In Sec. II, we give a brief outline of the definition of these global variables and their equations of motion and offer the reader the relevant references with thorough approaches.

In Sec. III we discuss the technical issues of the numerical setup. The relationship between spin weighted and tensorial spherical harmonics is used to link the gravitational radiation of the repository with the equations of motion for the global variables.

In Sec. IV we present some results that show the global behavior of these classes of binaries. The center of mass trajectories for selected members of the six classes are given, the tilt and change of the angular momenta are obtained for all cases, and kickback velocities are also computed. The results obtained from our equations of motion are consistent with those in the Rochester metadata.

II. EQUATIONS OF MOTION FOR THE CENTER OF MASS AND INTRINSIC ANGULAR MOMENTUM

There are many results that are needed for this work. In this section, we introduce several of the key ideas and the basic tools that are useful for our later discussion.

---

[*]emmanuel.tassone@unc.edu.ar

A. Asymptotically flatness and $\mathcal{I}^+$

We assume our spacetime is empty except for a bounded region where the dynamical interaction of the sources of gravitational radiation takes place. For such spacetimes there is a well-known mathematical structure where a null boundary $\mathcal{I}^+$ is added together with an appropriate definition of global variables that take into account the time evolution of the sources. In a neighborhood of $\mathcal{I}^+$ the gravitational field is given by the Weyl tensor. In the neighborhood of null infinity, it is also possible to introduce a particular system called Bondi system. A Bondi system is an inertial frame in general relativity, whose coordinates are labeled by $(u_B, r_B, \zeta_B, \bar{\zeta}_B)$. The time u_B represent null surfaces, r_B is the affine parameter along the null geodesics of the constant u_B surfaces and $\zeta_B, \bar{\zeta}_B$ are the complex stereographic coordinates.

Using a null tetrad adapted to a Bondi system one defines five complex scalars, whose asymptotic behavior is [10]

$$\psi_0 = C_{abc}{}^d m^a l^b l^c m_d \simeq \frac{\psi_0^0}{r_B^5},$$

$$\psi_3 = C_{abc}{}^d l^a n^b n^c \bar{m}_d \simeq \frac{\psi_3^0}{r_B^2},$$

$$\psi_1 = C_{abc}{}^d n^a l^b l^c m_d \simeq \frac{\psi_1^0}{r_B^4},$$

$$\psi_4 = C_{abc}{}^d \bar{m}^a n^b n^c \bar{m}_d \simeq \frac{\psi_4^0}{r_B},$$

$$\psi_2 = \frac{1}{2}(C_{abc}{}^d l^a n^b m^c \bar{m}_d - C_{abcd} l^a n^b l^c n_d) \simeq \frac{\psi_2^0}{r_B^3}.$$

With help of the peeling theorem, which describes the asymptotic behavior of the Weyl tensor, the radial part of the Einstein equations can be integrated leaving only the Bianchi identities at $\mathcal{I}^+$ as the unsolved equations. In a Bondi frame the resulting equations look remarkably simple. Some of those equations relate the Weyl scalars with the Bondi shear, i.e., [6,10]

$$\psi_2^0 + \eth^2 \bar{\sigma}^0 + \sigma^0 \dot{\bar{\sigma}}^0 = \bar{\psi}_2^0 + \bar{\eth}^2 \sigma^0 + \bar{\sigma}^0 \dot{\sigma}^0, \tag{1}$$

$$\psi_3^0 = \eth \dot{\bar{\sigma}}^0, \tag{2}$$

$$\psi_4^0 = -\ddot{\bar{\sigma}}^0. \tag{3}$$

Here the operator $\eth$ is known as the "eth operator" and is basically the complex covariant derivative over S^2 in stereographic coordinates. The derivative is taken at $u_B = $ const surfaces [11].

Finally, the Bianchi identities (in Bondi coordinates) at $\mathcal{I}^+$ are given by [6,10]

$$\dot{\psi}_0^0 = -\eth \psi_1^0 + 3\sigma^0 \psi_2^0, \tag{4}$$

$$\dot{\psi}_1^0 = -\eth \psi_2^0 + 2\sigma^0 \psi_3^0, \tag{5}$$

$$\dot{\psi}_2^0 = -\eth \psi_3^0 + \sigma^0 \psi_4^0. \tag{6}$$

Note that Eq. (1) defines a real variable Ψ called the mass aspect [12].

$$\Psi = \psi_2^0 + \eth^2 \bar{\sigma}^0 + \sigma^0 \dot{\bar{\sigma}}^0. \tag{7}$$

In term of Ψ is possible to write the Bondi mass M and Bondi lineal momentum P^i by

$$M = -\frac{c^2}{8\pi\sqrt{2}G} \int \Psi dS, \tag{8}$$

$$P^i = -\frac{c^3}{8\pi\sqrt{2}G} \int \Psi \tilde{l}^i dS, \tag{9}$$

with

$$\tilde{l}^i = \frac{1}{1 + \zeta\bar{\zeta}}(\zeta + \bar{\zeta}, -i(\zeta - \bar{\zeta}), 1 - \zeta\bar{\zeta}), \tag{10}$$

where $dS = \frac{4d\zeta \wedge d\bar{\zeta}}{P_0^2}$ is the area element on the unit sphere, and where i, j, k, l, $m = 1$, 2, 3 are three-dimensional Euclidean indices.

It is also quite convenient to give the evolution equation for Ψ. Directly from (6) one obtains

$$\dot{\Psi} = \dot{\sigma}^0 \dot{\bar{\sigma}}^0. \tag{11}$$

The above equation and (6) contain identical information.

B. Center of mass and intrinsic angular momentum

The center of mass and intrinsic angular momentum are useful concepts for isolated systems in general relativity. One can obtain global features from binary coalescence such as the kickback velocity, reaction radiation force, and angular momentum loss, among other physical quantities. Following a formulation presented several years ago [7], to obtain such variables, we first introduce special congruences of generalized Newman-Unti (NU) cuts at null infinity

$$u_B = Z(x^a(u), \zeta, \bar{\zeta}),$$

with $x^a(u)$ an arbitrary worldline in a fiducial Minkowski space. The above equation has a geometrical kinematical meaning. It represents the intersection of the future light cone of each point $x^a(u)$ with Scri and it is called a null cone cut congruence. In general, these cuts have caustics, but it is possible to construct the so-called regularized null cone cut congruences with a well-defined procedure that yields regular cuts at null infinity. In flat spacetime, the regularized cuts are given by

$$Z_0 = t(u) - \frac{1}{2} x^i(u) Y^0_{1i}, \tag{12}$$

where $Y^0_0, Y^0_{1i}, Y^0_{2ij}$ are the tensorial spin-s harmonic [13], and $x^a(u)$ an arbitrary worldline in Minkowski spacetime. The linearized deviation from flat space is given by [8],

$$Z_1 = Z_0 + \left(\frac{\Delta \sigma^{ij}_R}{12} + \frac{1}{72} \dot{\sigma}^{ig}_I x(u)^f \epsilon^{gfi} \right) Y^0_{2ij}, \tag{13}$$

where the extra term is the quadrupolar contribution of the Bondi shear with $\Delta \sigma^{ij}_R$ the deviation from the initial real part of the shear. $\dot{\sigma}^{ig}_I$ is the derivative with respect to Bondi time of the shear imaginary part and ϵ^{gfi} is the Levi-Civita symbol. The extra term in (13) explicitly depends on the gravitational radiation and it vanishes for a stationary situation. If $x^a(u)$ describes any worldline, then Z_1 describes a NU foliation up to the order needed for this calculation. From the geometrical meaning outlined before, the above equation represents NU congruences parametrized by worldlines in a Minkowski spacetime. This fiducial flat space will be used to write down the equations of motion for the center of mass and intrinsic angular momentum.

We then use the Winicour linkages [14] to define the notion of dipole mass moment and angular momentum on these null cone cut congruences from the real and imaginary parts of the linkage integral as follows [7,12],

$$D^{*i} + ic^{-1}J^{*i} = -\frac{c^2}{12\sqrt{2}G} \left[\frac{2\psi^0_1 - 2\sigma^0 \eth \bar{\sigma}^0 - \eth(\sigma^0 \bar{\sigma}^0)}{Z'^3} \right]^{*i}. \tag{14}$$

The reader should here distinguish between the i labeling the index of the equation and the i multiplying the factor c^{-1}, which is the imaginary unit. This latter i will no longer appear after we separate the equation into its real and imaginary part.

Finally, we assume that among all possible null cone cut congruences, there exists a special worldline $R^a(u)$ such that at each $u = \text{const}$ cut the mass dipole moment D^{*i} vanishes. This special worldline will be called the center of mass worldline of the system. The angular momentum J^{i*} evaluated at the center of mass will be the intrinsic angular momentum S^i.

From the point of view of Bondi observers for each $u = \text{const}$ cut, there exist a Lorentz boost and a translation that relate the above defined variables to the equivalent definitions given on Bondi cuts; i.e., if we define D^i and J^i in a Bondi system as

$$D^i + ic^{-1}J^i = -\frac{c^2}{12\sqrt{2}G} [2\psi^0_1 - 2\sigma^0 \eth \bar{\sigma}^0 - \eth(\sigma^0 \bar{\sigma}^0)]^i, \tag{15}$$

then the transformation law between the quantities $(\psi^{0*}_1, \sigma^{0*}, \eth)$ and $(\psi^0_1, \sigma^0, \eth_B)$ together with the condition that in the center of mass foliation the dipole mass moment vanishes, i.e., $D^{i*}|_{u=\text{const}} = 0$, yields the relativistic definition of center of mass worldline. The details can be found in Refs. [7,12]. The final results read

$$D^i = MR^i + \frac{1}{c^2} \epsilon^{ijk} V^j S^k - \frac{8}{5\sqrt{2}c} P^j \Delta \sigma^{ij}_R$$
$$- \frac{c^2}{G} \epsilon^{ijk} \left(\frac{4}{5} \sigma^{jl}_I \sigma^{kl}_R - \frac{36}{7} \sigma^{klm}_I \sigma^{jlm}_R \right), \tag{16}$$

$$J^i = S^i + \epsilon^{ijk} R^j P^k - \frac{151 c^2}{168\sqrt{2}G} (\sigma^{ijk}_R \sigma^{jk}_I - \sigma^{ijk}_I \sigma^{jk}_R), \tag{17}$$

where the above equations have been written keeping up to linear terms in the velocity and up to second order in the radiation fields. We have only kept quadrupole and octupole terms in the Bondi shear since these terms capture the main part of the gravitational radiation given in the repository.

The main contribution to the gravitational radiation comes from the $l = 2$ and $l = 3$ spherical harmonic decomposition.

The above equations relate the center of mass R^i and intrinsic angular momentum S^j with the asymptotic variables D^i, M, P^i, and J^i, given on a Bondi coordinate system. Note also that $V^i = \frac{1}{\sqrt{2}} \dot{R}^i$ since the relativistic time is $t = u\sqrt{2}$.

We list in Eqs. (18)–(21) the evolution equations of the Bondi physical variables that are needed for this work. The evolution equations of D^i and J^i follow from the Bianchi identity for ψ^0_1 when the $\ell = 1$ component of the real and imaginary parts of $\dot{\psi}^0_1$ is computed [8]. Furthermore, the dynamical evolution of the Bondi mass M and momentum P^i can be computed from the Bianchi identity for $\dot{\psi}^0_2$. These equations are given by

$$\dot{D}^i = \sqrt{2}P^i + \frac{3}{7} \frac{c^2}{\sqrt{2}G} [(\dot{\sigma}^{ijk}_R \sigma^{jk}_R - \sigma^{ijk}_R \dot{\sigma}^{jk}_R)]$$
$$+ \frac{3}{7} \frac{c^2}{\sqrt{2}G} [(\dot{\sigma}^{ijk}_I \sigma^{jk}_I - \sigma^{ijk}_I \dot{\sigma}^{jk}_I)], \tag{18}$$

$$\dot{J}^i = \frac{c^3}{5G} (\sigma^{kl}_R \dot{\sigma}^{jl}_R + \sigma^{kl}_I \dot{\sigma}^{jl}_I) \epsilon^{ijk}$$
$$+ \frac{9c^3}{7G} (\sigma^{klm}_R \dot{\sigma}^{jlm}_R + \sigma^{klm}_I \dot{\sigma}^{jlm}_I) \epsilon^{ijk}, \tag{19}$$

$$\dot{M} = -\frac{c}{10\sqrt{2}G} (\dot{\sigma}^{ij}_R \dot{\sigma}^{ij}_R + \dot{\sigma}^{ij}_I \dot{\sigma}^{ij}_I)$$
$$- \frac{3c}{7\sqrt{2}G} (\dot{\sigma}^{ijk}_R \dot{\sigma}^{ijk}_R + \dot{\sigma}^{ijk}_I \dot{\sigma}^{ijk}_I), \tag{20}$$

$$\dot{P}^i = \frac{2c^2}{15\sqrt{2}G}\dot{\sigma}_R^{jl}\dot{\sigma}_I^{kl}\epsilon^{ijk} - \frac{\sqrt{2}c^2}{7\sqrt{2}G}(\dot{\sigma}_R^{jk}\dot{\sigma}_R^{ijk} + \dot{\sigma}_I^{jk}\dot{\sigma}_I^{ijk})$$

$$+ \frac{3c^2}{7\sqrt{2}G}\dot{\sigma}_R^{jlm}\dot{\sigma}_I^{klm}\epsilon_{ijk}. \tag{21}$$

The main idea then is to give initial data to solve for Eqs. (18)–(21), assuming that before the gravitational radiation is emitted the center of mass world line is the origin of a Bondi coordinate system. Once the Bianchi identities have been solved we introduce a perturbation procedure that preserves the order of the equations and algebraically solve for R^i and S^j.

It is worth noting that the equations of motion are written in terms of the Bondi shear whereas the gravitational radiation is given by ψ_4^0. To find the relationship between those scalars we first write [15]

$$\psi_4^0 = \sum_{l,m}\Psi^{lm}{}_{(-2)}Y_{lm}. \tag{22}$$

Here Ψ^{lm} represents the multipole of the gravitational wave at infinity. In practice, Ψ^{lm} are functions stored in data files generated by the numerical simulation of the astrophysical systems such as the binary coalescence of black holes [16].

We then use Eq. (3) to write

$$\ddot{\bar{\sigma}}^0 = -\sum_{l,m}\Psi^{lm}{}_{(-2)}Y_{lm}. \tag{23}$$

Integrating twice the above equation one obtains the real and imaginary parts of the Bondi shear. Usually one assumes the real part of the shear vanishes initially, but it is just a matter of convenience since the equations are supertranslation invariant. Also, in many works in GR, it is usual to expand the shear, and other scalars, in terms of the tensorial harmonics as follows (cf. [13]):

$$\sigma^0 = \sigma^{ij}Y_{2ij}^2 + \sigma^{ijk}Y_{3ijk}^2 + \cdots, \tag{24}$$

$$\ddot{\bar{\sigma}}^0 = \ddot{\bar{\sigma}}^{ij}Y_{2ij}^{-2} + \ddot{\bar{\sigma}}^{ijk}Y_{3ijk}^{-2} + \cdots, \tag{25}$$

where σ^{ij} and σ^{ijk} are related to the quadrupole and octupole contribution of the gravitational wave, respectively. On the other hand, the spin weighted spherical harmonic decomposition is often used in the literature of gravitational radiation. Thus, to be able to find the evolution of R^i and S^j one must first obtain a correspondence between $Y_{2ij}^{-2} \rightarrow {}_{(-2)}Y_{2m}$ and $Y_{2ijk}^{-2} \rightarrow {}_{(-2)}Y_{3m}$ (see [17]) and then solve for $\ddot{\bar{\sigma}}^{ij}$. This is further discussed in the next section. The relevant components of the shear needed for this work are given by

$$\ddot{\bar{\sigma}}^{xy} = -\frac{i}{4}\sqrt{\frac{5}{\pi}}(\Psi^{22} - \Psi^{2-2}), \tag{26}$$

$$\ddot{\bar{\sigma}}^{xx} = -\frac{1}{4}\sqrt{\frac{5}{\pi}}(\Psi^{2-2} + \Psi^{22}) + \frac{1}{6}\sqrt{\frac{15}{2\pi}}\Psi^{20}, \tag{27}$$

$$\ddot{\bar{\sigma}}^{yy} = \frac{1}{4}\sqrt{\frac{5}{\pi}}(\Psi^{2-2} + \Psi^{22}) + \frac{1}{6}\sqrt{\frac{15}{2\pi}}\Psi^{20}, \tag{28}$$

$$\ddot{\bar{\sigma}}^{yz} = \frac{i}{4}\sqrt{\frac{5}{\pi}}(\Psi^{2-1} + \Psi^{21}), \tag{29}$$

$$\ddot{\bar{\sigma}}^{xz} = \frac{1}{4}\sqrt{\frac{5}{\pi}}(\Psi^{21} - \Psi^{2-1}), \tag{30}$$

and

$$\ddot{\bar{\sigma}}^{xxx} = \frac{1}{8}\sqrt{\frac{7}{5\pi}}(\Psi^{3-1} - \Psi^{31}) + \frac{1}{8}\sqrt{\frac{7}{3\pi}}(\Psi^{33} - \Psi^{3-3}), \tag{31}$$

$$\ddot{\bar{\sigma}}^{xyy} = \frac{1}{24}\sqrt{\frac{7}{5\pi}}(\Psi^{3-1} - \Psi^{31}) - \frac{1}{8}\sqrt{\frac{7}{3\pi}}(\Psi^{33} - \Psi^{3-3}), \tag{32}$$

$$\ddot{\bar{\sigma}}^{yyy} = -\frac{i}{8}\sqrt{\frac{7}{5\pi}}(\Psi^{3-1} + \Psi^{31}) - \frac{i}{8}\sqrt{\frac{7}{5\pi}}(\Psi^{33} + \Psi^{3-3}), \tag{33}$$

$$\ddot{\bar{\sigma}}^{xxy} = -\frac{i}{24}\sqrt{\frac{7}{5\pi}}(\Psi^{3-1} + \Psi^{31}) + \frac{i}{8}\sqrt{\frac{7}{5\pi}}(\Psi^{33} - \Psi^{3-3}), \tag{34}$$

$$\ddot{\bar{\sigma}}^{xxz} = -\frac{1}{12}\sqrt{\frac{7}{2\pi}}(\Psi^{32} + \Psi^{3-2}) + \frac{1}{4}\sqrt{\frac{7}{15\pi}}\Psi^{30}, \tag{35}$$

$$\ddot{\bar{\sigma}}^{yyz} = \frac{1}{12}\sqrt{\frac{7}{2\pi}}(\Psi^{32} + \Psi^{3-2}) + \frac{1}{4}\sqrt{\frac{7}{15\pi}}\Psi^{30}, \tag{36}$$

$$\ddot{\bar{\sigma}}^{xyz} = \frac{i}{12}\sqrt{\frac{7}{2\pi}}(\Psi^{3-2} - \Psi^{32}). \tag{37}$$

III. THE NUMERICAL EVOLUTION

In this section we explain how the time evolution is made. The idea is basically to obtain the sigma tensors in which our formalism is described. We thus use the set of equations derived from the Bianchi identities at null infinity presented in (18)–(21). They are valid in any Bondi frame and can be numerically integrated to obtain their time evolution.

A. A dictionary between tensorial and spin weighted spherical harmonics

The solutions of Eqs. (18)–(21) are then used to algebraically solve for the center of mass R^i and intrinsic angular momentum S^i. In order to obtain the mass dipole moment, the angular momentum and the linear momentum, we need only the 2 and 3 modes of Ψ^{lm} (taken from [18]) to

get the values of the shear components shown above. Higher order modes correspond with higher order tensor decomposition of sigmas, and thus $l = 4$ modes are irrelevant for the precision order to which our formulation applies.

As a first step, we establish a relationship between the spin weighted spherical harmonics used in the catalog and the tensorial spherical harmonics used in the definitions of R and S.

To expand the Weyl scalar ψ_4 of the Newman-Penrose formalism [6,7,12] and to map the tensorial Bondi shear into the multipole associated with the gravitational wave we use the one-to-one correspondence between tensorial spin-s harmonics denoted by $Y^{(s)}_{(l)i...k}$ [13] and the spin-weighted spherical harmonics $_{(s)}Y_{lm}$. This correspondence was shown in [17].

B. Sigma calculus

Obtaining the Bondi shear implies integrating twice the scalar ψ_4. There is a well-known nonlinear drift that appears as a secular effect coming from the double integration [19,20]. On top of this there is also a linear drift coming from the initial values of σ_B and $\dot\sigma_B$ that must be given in the integration. These drifts must be corrected in order to obtain a more accurate shear and thus more accurate final parameters of the evolution.

Reisswig [20] has implemented a code to deal with those problems performing the Fourier transformation with a windowing function and a low-frequency cutoff (which should be lower than all physically possible frequencies) [21]. The code provides the strain of the gravitational radiation, commonly denoted in the literature as h.

For the purpose of this work, which is to check qualitatively the consistency of the Kozameh-Quiroga formalism, it is understandable to disregard the drifts for a first overview of the formalism. In Figs. 1(a) and 1(b) we show the difference from integrating with Reisswig code (blue dotted line) and making an integration directly (orange solid line). Note that the plot is in terms of the quantity σ, which is not directly obtained by the code but is easy to obtain with the relation $h = -\sigma$, where h is the strain and σ the shear we use along all this writing. The drifts produce a change of order ~ 0.2 at most (largest component σ). Moreover, Eqs. (21) and (20) are quadratic on σ_{ij} hence making the drift effect smaller (~ 0.04). This will be the case for the majority of simulations also. The incorporation of this effect is left for a future and more accurate study.

C. Getting rid of traveling waves

Another problem we address is how to get rid of traveling waves that are present on any initial dataset. We take as an example the evolution of the 0443 simulation whose gravitational radiation is plotted in Fig. 2. We plot the square root of the integral of $\Psi_4^0 \overline{\Psi}_4^0$ on the sphere to take
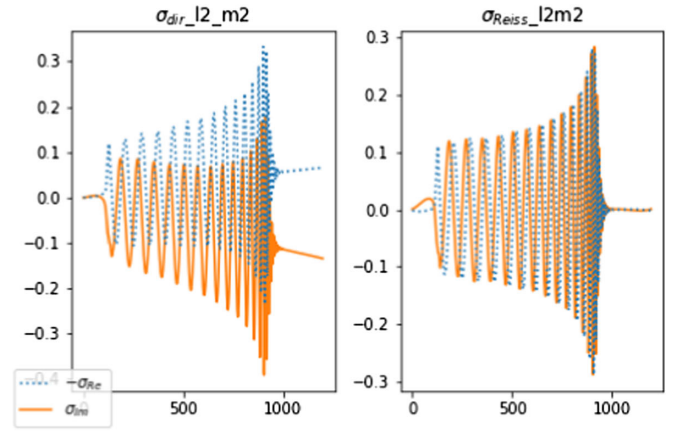
(a) Comparison of modes l=2,m=2.
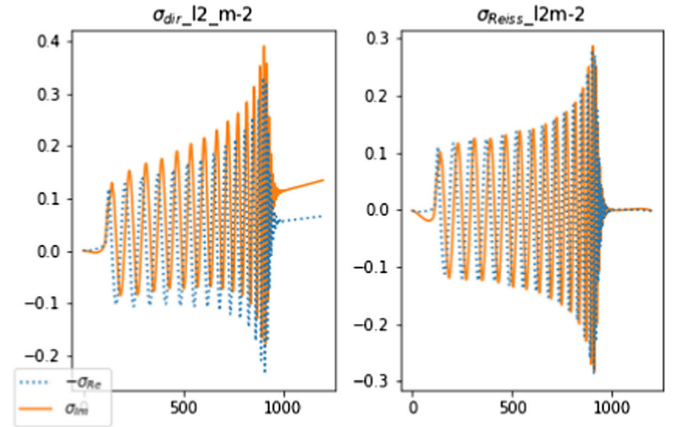
(b) Comparison of modes l=2,m=-2.

FIG. 1. Integration of the modes that made the most important contribution to simulation 0014. On the left σ_{dir} are the plots of integrating directly. On the right, σ_{Reiss} are the sigmas obtained when Reiss code is implemented.
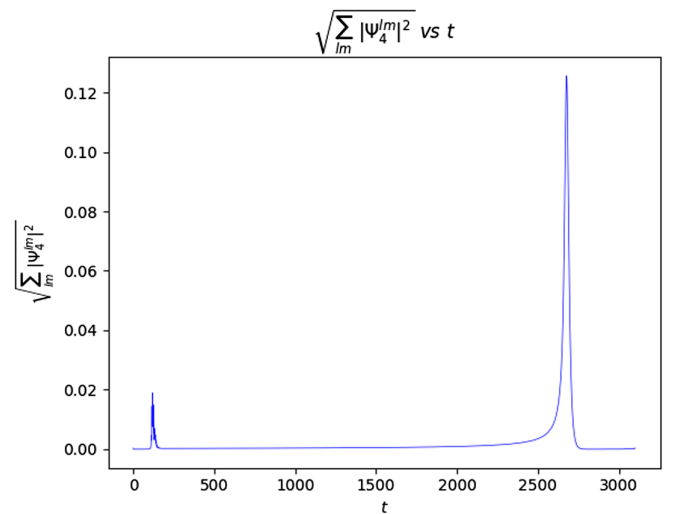

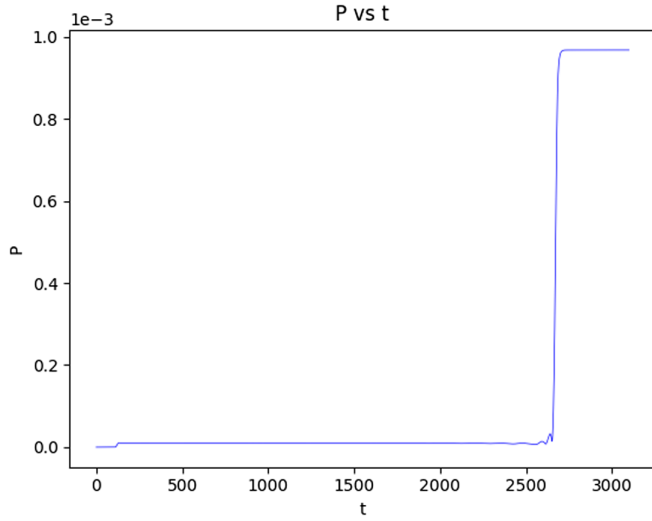FIG. 2. Evolution of the gravitational radiation for the simulation case 0443.

FIG. 3. Time evolution of the magnitude of the Bondi momentum. A small change between 0 and 500 due to the traveling wave can be seen.

into account the different contributions of the $l = 2$ and $l = 3$ terms. One can see a traveling wave that is not relevant for the coalescence problem at the beginning of the time evolution. This will produce an unwanted jump of the Bondi linear momentum.

The Fig. 3 shows the evolution of the Bondi momentum using the Rochester repository on a Bondi frame whose origin is at the center of mass which is initially at rest. After the traveling wave passes by, the momentum is no longer zero and remains constant until the gravitational wave of the binary system is emitted. After that the Bondi momentum is constant and nonvanishing. Since a traveling wave is an unwanted and generic feature of any numerical simulation we run the codes until a relaxation time is reached before the binary coalescence. We then reset the time and select another Bondi frame at rest with the center of mass at that time.

D. The numerical setup

We first perform the numerical integration of $\dot{M}$ (20), $\dot{P}^i$ (21), $\dot{D}^i$ (18), and $\dot{J}^i$ (19), where the initial values for those variables are taken from the metadata repository. The unwanted solitary waves that are present in any numerical integration are subtracted by finding the relaxation time (time where the wave is completely gone) and then subtracting the contribution of the traveling wave to the gravitational radiation at null infinity. Essentially this amounts to resetting the initial time to the relaxation time and then using the Rochester data as the initial data for the evolution equations. Our Bondi system is such that at the relaxation time the origin of our coordinates is at the center of mass, which is at rest at that time. The initial time is then reset to zero.

We then algebraically solve for

$$MR^i + c^{-2}\epsilon^{ijk}\frac{P^j}{M}S^k = D^i + \frac{8}{5\sqrt{2}c}P^j\Delta\sigma_R^{ij}$$
$$+ \frac{c^2}{G}\epsilon^{ijk}\left(\frac{4}{5}\sigma_I^{jl}\sigma_R^{kl} - \frac{36}{7}\sigma_I^{klm}\sigma_R^{jlm}\right) \tag{38}$$

and

$$S^i + \epsilon^{ijk}R^jP^k = J^i + \frac{151c^3}{168\sqrt{2}G}(\sigma_I^{jk}\sigma_R^{ijk} - \sigma_I^{ijk}\sigma_R^{jk}). \tag{39}$$

Where we have kept a first order expression of V^i from the Bianchi identity of $\dot{D}^i$ (18).

IV. RESULTS

Following the conventions of the Rochester repository, we have divided the numerical outcomes in different classes according to the relative masses into EM or NEM. Likewise, the spins of the black holes are taken into account and we can distinguish between NS ones, which are aligned with the orbital angular momentum or precessing spins. Thus an EM-P simulation has two black holes with equal mass and precessing spins nonaligned with the orbital angular momentum.
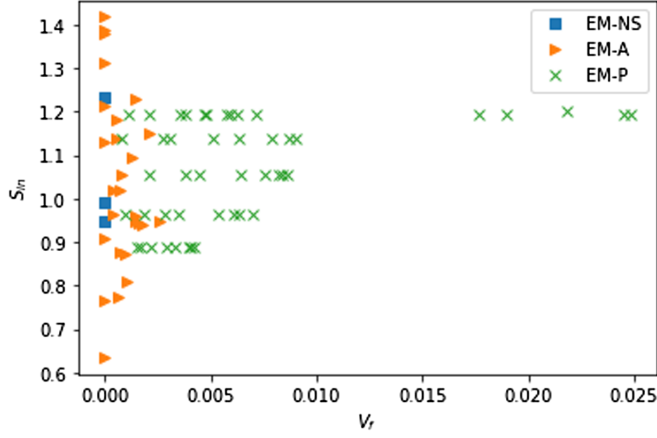
A. Data analysis

1. A relationship between the initial angular momentum and the kickback velocity

We plot below the relationship between the initial angular momentum and the final velocity for two classes of initial data, EM and NEM.

We can see a clear difference between the precessing and nonprecessing cases in each class. The precessing binaries attain the highest final velocities, although they are highly spread for the same values of initial angular momentum. The reason for the wide range of final velocities in the P cases lies in the intrinsic chaotic behavior of the precessing BHs.

One can see that there are only three simulations in Fig. 4(a) for the EM-NS case. The center of mass in those simulations does not acquire velocity as one might have guessed. The NEM-NS cases yield small and nonchaotic final kicks. For the aligned cases the final velocities are small and densely distributed, showing a nonchaotic behavior.

It is worth mentioning Figs. 4(a) and 4(b) seem to achieve a peak for the final velocities in some range of initial S_{in} depending on the classes. Nevertheless, this effect could be biased due to the much fewer number of simulations for the values $S_{\text{in}} > 1.2$.

(a) Final velocities for the EM class.
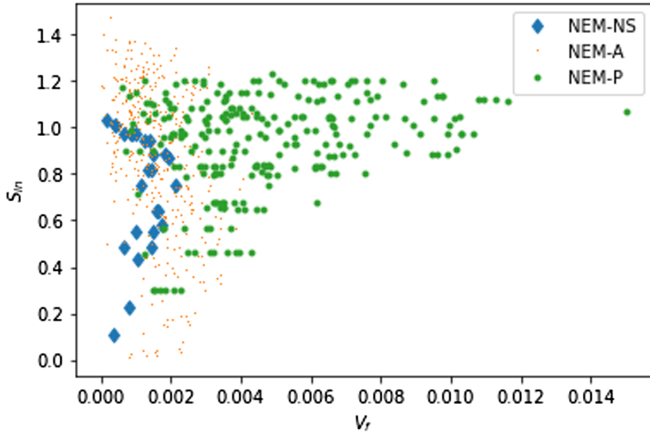
(b) Final velocities for the NEM class.

FIG. 4. Initial angular momentum vs final velocity.

2. A relationship between the magnitudes of the initial and final angular momenta

The loss of orbital angular momentum Fig. 5 shows up for both the EM-NS, and the NEM-NS cases. The NEM-A class has a wide range of outcomes and in some cases the final angular momentum increases when the initial angular momentum is very close to zero. This special feature occurs when the spins are antialigned with the orbital angular momentum. Whereas the magnitude of the orbital part always decreases, the total angular momentum goes up since the spins remain approximately constants. We made a Fig. 5 fit of the final values obtained for all the classes to get a representative value of the outcomes for the simulations. This should not be regarded as the exact relation between J_{in} and J_f, which is described by Eq. (19).

3. The change in direction of the intrinsic angular momentum

To calculate the change in direction of the angular momentum we use the usual scalar product between the initial vector J_i and the final J_f:
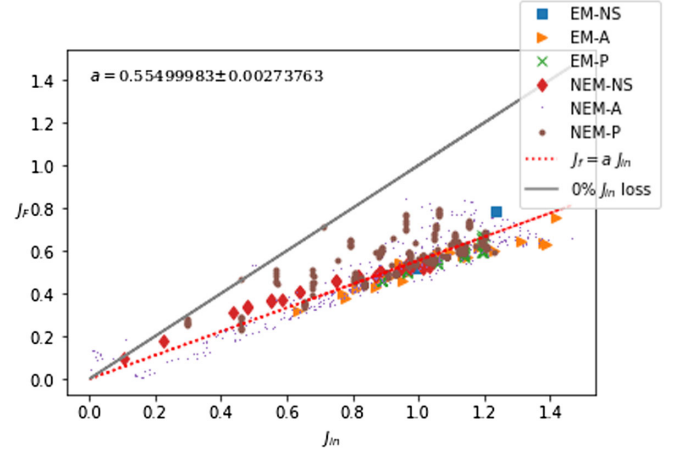

FIG. 5. A relationship between the magnitudes of the initial and final angular momenta.

$$\Delta\theta = \frac{\mathbf{J}_f \cdot \mathbf{J}_i}{|\mathbf{J}_f||\mathbf{J}_i|}, \tag{40}$$

where $\mathbf{J}_i$ in this particular case is the angular momentum at the relaxation time and $\mathbf{J}_f$ is the angular momentum at the final time of the evolution. $\mathbf{J}_i$ is here chosen in such a way to avoid the contribution of the traveling wave to the tilting angle. Thus we use the following definition at relaxation time

$$\mathbf{J}_i = \mathbf{L}_{ni} + \mathbf{S}_{1i} + \mathbf{S}_{2i}, \tag{41}$$

where $\mathbf{L}_{ni}$, $\mathbf{S}_{1i}$, $\mathbf{S}_{2i}$ are the orbital angular momentum and the spin of the first and second components at relaxation time, respectively. Hence, initial angular momentum is defined as Newtonian angular momentum since there is no radiation at that particular time. Given the above, Fig. 6 shows that NS systems have vanishing tilt. A similar situation occurs for the EM-A subclass whereas the NEM-A exhibit a small tilt. Overall, we see a tendency of the aligned and nonspinning configurations to have a
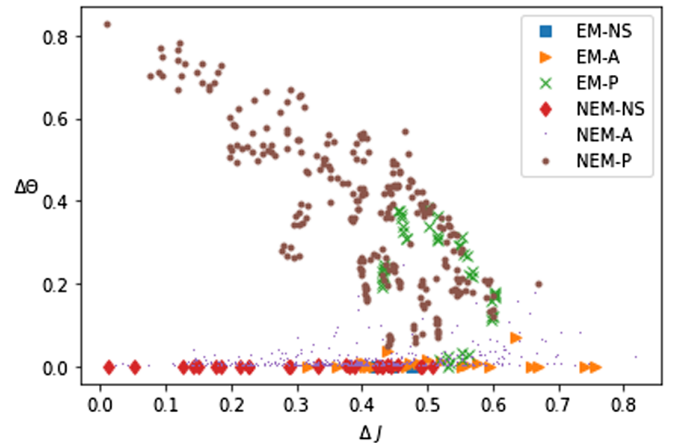

FIG. 6. A relationship between the change in the magnitude of the angular momenta and the tilting angle.

tilting angle ~ 0, which we attribute to the known fact these configurations are stable ones [22].

On the contrary, preccesing systems are known to be chaotic. The most interesting cases are the P types, which have a wide range of tilting angles. In particular, the tilting angle in NEM-P subclass appears to be inversely proportional to the change of angular momentum, the smaller the change in magnitude of S, the bigger the tilt. Whether the EM-P exhibit a similar behavior is unknown due to the lack of simulation in the same range as NEM-P.

Finally we remark that, despite we calculate the change of the tilting angle using the total angular momentum at the relaxed and final time, it is important to note that the tilting angle is the same for the intrinsic angular momentum S. Indeed, at those times $\sigma \sim 0$ as there is no radiation at relaxation time and after the coalescence. Further, $\mathbf{R} \times \mathbf{P} \sim 0$ for the plot order in Fig. 14, making $J_i = S_i$ and $J_f = S_f$.

4. Correlation between the gravitational kick and the final value of P^i/M

After selecting the new Bondi frame we run the codes using the values for M and S at the relaxation time and vanishing position and velocity for the center of mass. Since the center of mass position is obtained algebraically and then numerically derived to obtain the kickback velocity it is worthwhile to check its relationship with the final value of P^i/M.

Note that the Fig. 7 slope is $a = 1.02$. This 2% difference can be attributed to the fact that the numerical evolutions for P^i and M are affected by the linear drifts in σ, making a small contribution after the coalescence has taken place (see Sec. III B).

5. Relation between the radiation reaction force (F_R) and the gravitational radiation

It is relevant to plot the time evolution of the (magnitude of the) radiation reaction force and its relation with the different modes of Ψ_4. To do that we define
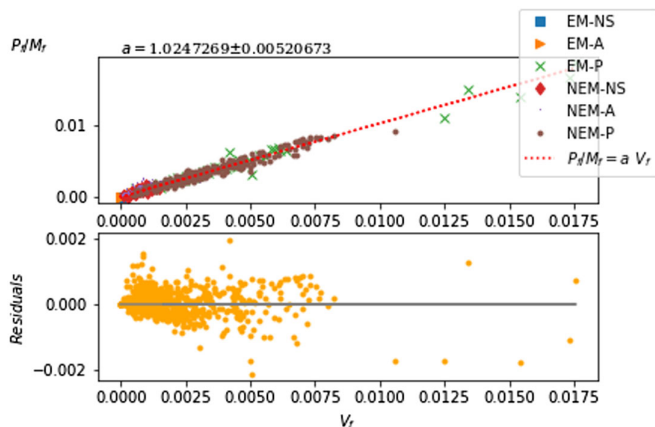

FIG. 7.   Correlation between V_f and $(P^i/M)_f$.

$$F_R^i = \frac{1}{\sqrt{2}} \frac{d(MV^i)}{du} \qquad (42)$$

and Fig. 8 plot its time evolution of the different cases. In this case we select the simulation number 0443, but a similar pattern is obtained by any of the cases obtained. We first plot the contributions of the different modes of Ψ_4, for the whole process and enlarging the coalescence interval to enhance the differences between the modes.

As we can see Fig. 8 in these graphs, each mode gives a different contribution and they even peak at different times. Thus, depending on the coalescing scenario, the magnitude and direction of the impulse given by the F_R can be quite different.
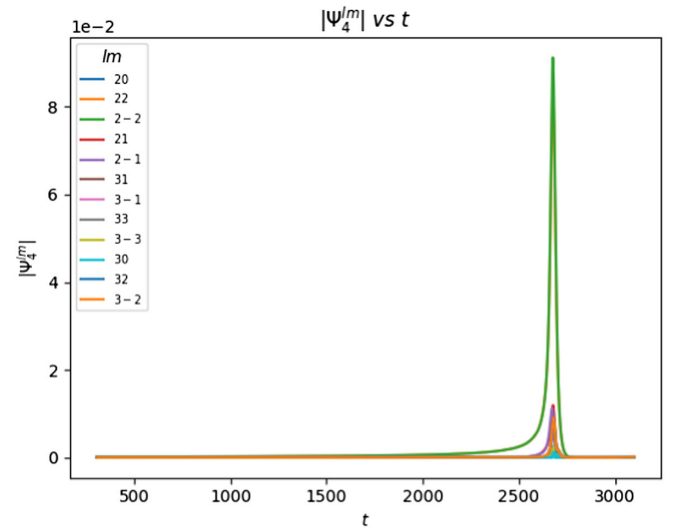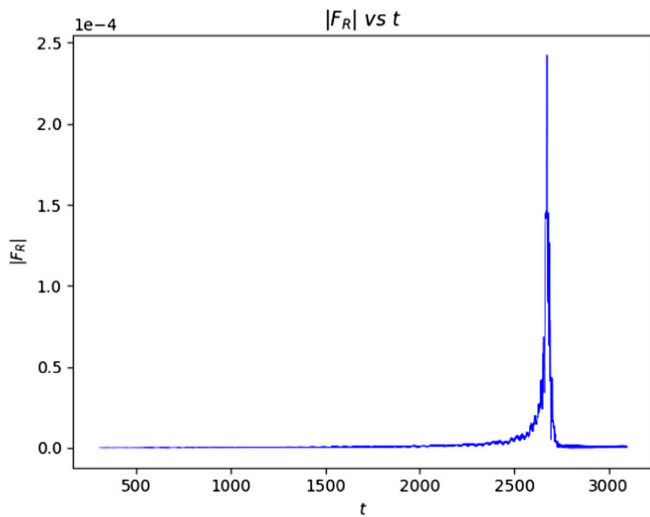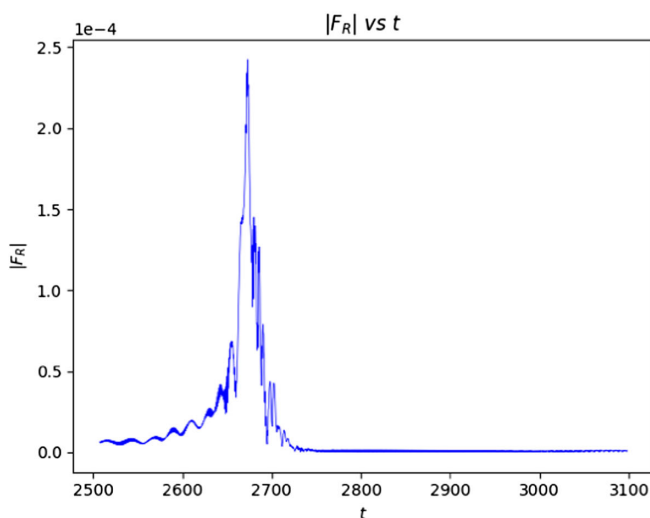

(a) Whole evolution of the different modes
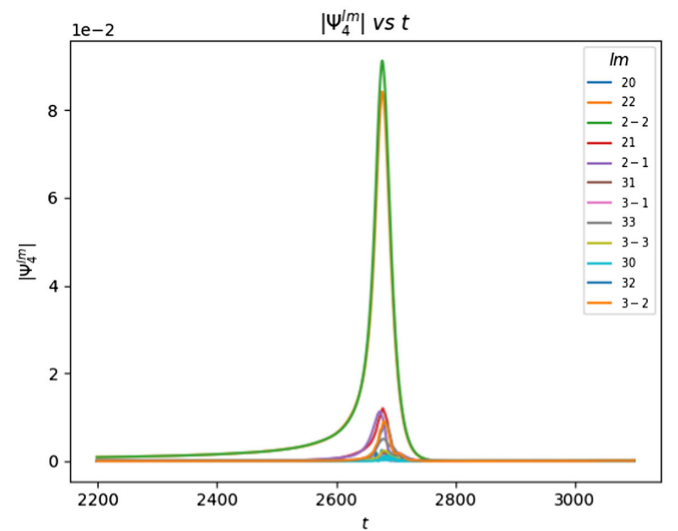
(b) Enlargement to enhance the differences

FIG. 8.   Time evolution of the different modes of Ψ_4.

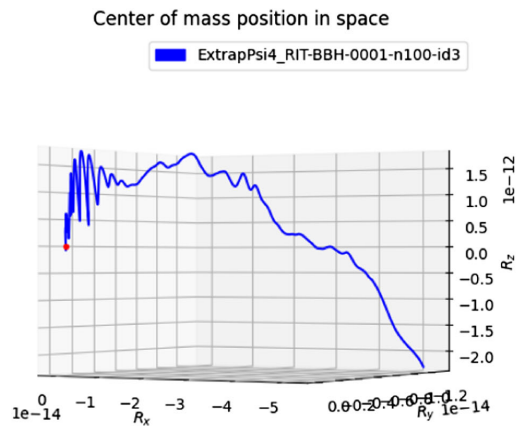(a) Whole evolution of F_R

(b) Enlargement to enhance the peak

FIG. 9.   Time evolution of the magnitude of F_R.

(a) 0001-EM-NS

(b) 0373-NEM-NS

FIG. 10.   Movement of the center of mass with aligned-spins binaries. The red dot specifies the starting point of the center of mass and the number above the plot indicates the simulation from the RIT catalog where ψ_4 has been taken.

In Fig. 9(b) we plot the magnitude of F_R for the 0443 case. In this case the F_R and the $l = 2$ modes of the gravitational radiation peak at the same time, but this can only be seen in the numerical data.
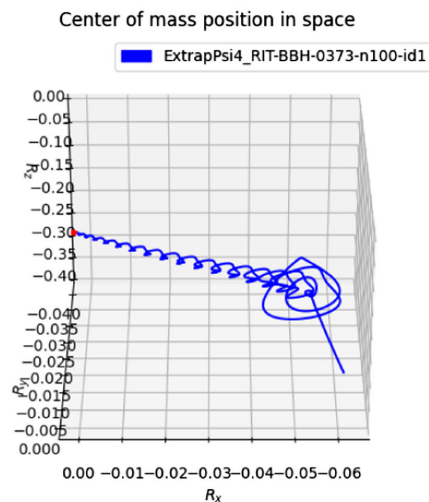
6. Some typical behaviors of the center of mass motion while emitting gravitational radiation

Finally, we plot the trajectory of the center of mass for selected representatives of each subclass.

Note the difference in the scale of both plots. In the EM-NS Fig. 10 case the center of mass remains virtually still and its final velocity is almost zero (1.3×10^{-13} or 0.039 mm/s). The NEM-NS is completely different, in this case the center of mass describes a spiral trajectory until the coalescing time, where it is ejected at a final speed of 5.5×10^{-04} or 165 km/s. In the EM-A Fig. 11 case the

center of mass remains virtually in the same place and after emitting radiation remains at rest (1.26×10^{-12} or 0.378 mm/s). In contrast to EM case, the center of mass in NEM-A case has a spiral trajectory that is noticeable at the end, and its final speed is 8.96×10^{-04} (269 km/s).

Both configurations of EM when the spin is static, i.e., aligned or nonspinning, present a null kick velocity, whereas when the masses are nonequal the final kick velocities are noticeable. This suggests that equal masses configuration (A or NS) are likely to be stable and thus end up with no kickback and angular momentum in the same direction.

In the precessing graphs, where the spins are not static, we observe a similar behavior between the EM or NEM cases, even though the former is slightly lower than the latter. The final speeds for the EM and NEM cases are 6.66×10^{-04} (200 km/s) and 1.18×10^{-03} (354 km/s),
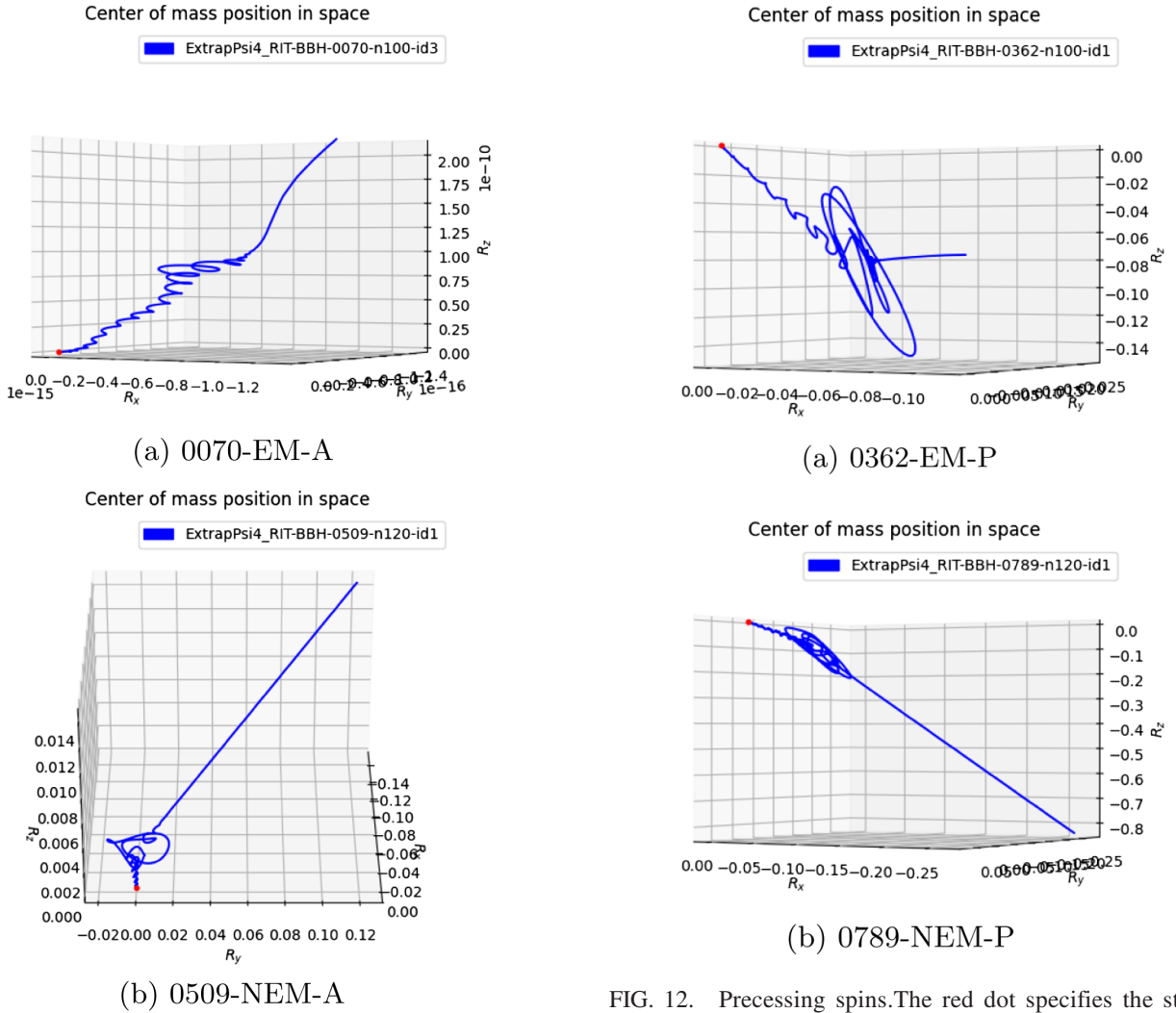
(a) 0070-EM-A

(b) 0509-NEM-A

FIG. 11. Movement of the center of mass with nonspinning binaries. The red dot specifies the starting point of the center of mass and the number above the plot indicates the simulation from the RIT catalog where ψ_4 has been taken.

(a) 0362-EM-P

(b) 0789-NEM-P

FIG. 12. Precessing spins. The red dot specifies the starting point of the center of mass and the number above the plot indicates the simulation from the RIT catalog where ψ_4 has been taken.

$$\Delta M_{\text{Roch}} = |M_F - M_{\text{relax}}| = M_{\text{relax}} - M_F, \qquad (43)$$

where M_F is the final mass of the Kerr black hole and M_{relax} is the mass at the relaxation time (which is slightly bigger than initial mass due to the traveling wave).

Plotting both ΔM leads to 13. We see there is a 20% difference from the ideal case. This could be attributed to the fact that defining (43) with M_{relax}, we are using a local measure of mass. This quantity should not differ too much from the asymptotic relaxed mass, as the only emitted radiation has been due to the travelling wave. Still, the effects discussed in Sec. III B can be another cause of this discrepancy.

respectively. We see the precessing spin plays an important role on increasing the kickback velocity in Fig. 12(a). This is a general feature of the class, as can be seen in Figs. 4(a) and 4(b).

B. Comparison with RIT catalog metadata

There are some scalar quantities listed as final parameters in Rochester metadata simulations. In this section we compare Rochester parameters with the result obtained by Eqs. (18)–(21). We show that they are consistent except for some difference in decimals, which we could be better at matching, making a more accurate evolution.

1. Correlation between mass variations

To compare the mass variation (20) we defined the Rochester mass change as

2. Correlation between angular momentum changes

In Fig. 14 we compare the variation ΔJ obtained in Eq. (19) with the angular momentum variation in Rochester metadata, which we define as
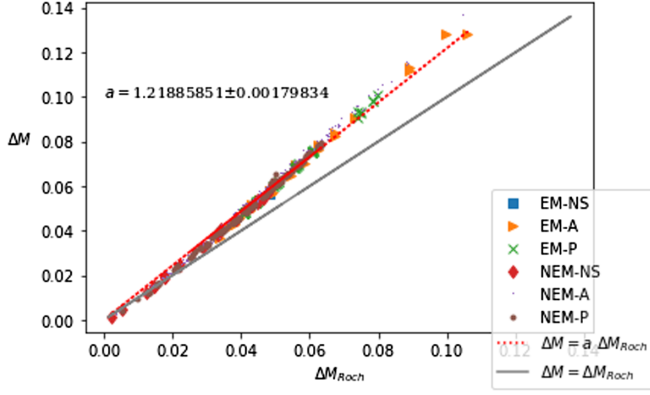
FIG. 13.   Correlation between ΔM and ΔM_{Roch}.
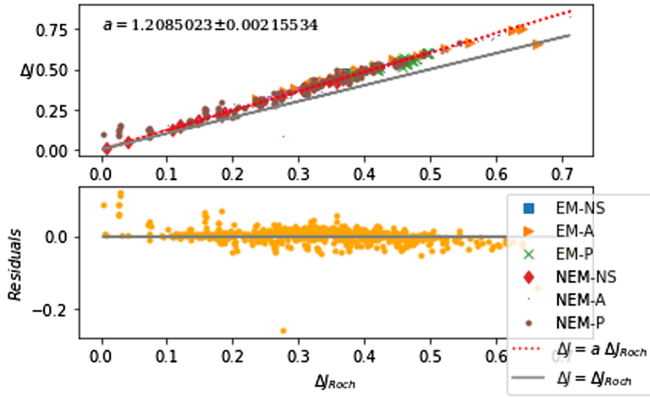
FIG. 14.   Correlation between ΔJ and ΔJ_{Roch}.

$$\Delta J = |\chi M^2 - J_{\mathrm{ADM}}|. \qquad (44)$$

The absolute value here makes ΔJ positive. We are using as definition of final angular momentum that of a Kerr black hole $J_f = \chi M^2$, where χ and M_f are the dimensionless spin parameter and the final mass of the resultant black hole, respectively. As the components of the final angular momentum from the black hole are not provided, we use definition (44), which gives the correct change for non-spinning and aligned configurations. Yet this definition does not coincide exactly with the angular momentum change for precessing configurations.

On the other hand, we subtract the absolute value of initial ADM angular momentum to estimate a change of the angular momentum. Note that making this subtraction we are considering the small contribution of the traveling wave to ΔJ_{Roch} in Fig. 14.

We end this section by showing the comparison of the obtained final angular momentum for the evolution equation (19). The correlation is shown in Fig. 15. J_F is defined as

$$J_f = |\mathbf{J}_F| = |\mathbf{J}_{\mathrm{ADM}} + \Delta \mathbf{J}|, \qquad (45)$$
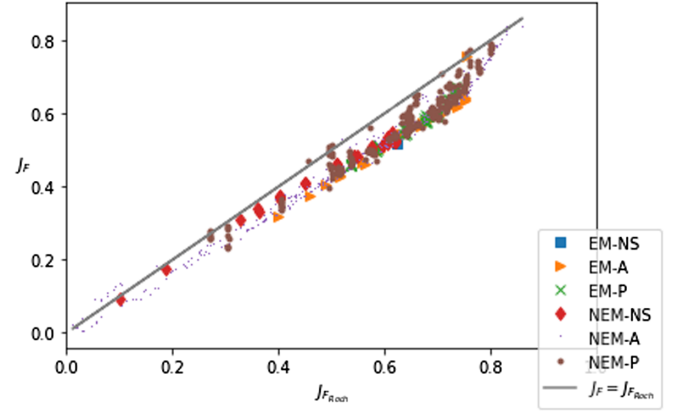

FIG. 15.   Correlation between the magnitude of final angular momenta.

with $\Delta \mathbf{J}$ being that obtained with (19). Again, $J_{F_{\mathrm{Roch}}}$ is defined as in (44). As $\mathbf{J}_{\mathrm{ADM}}$ is not the same for all the simulations, it is not trivial to expect a linear correlation of J_F and J_{Roch}. Whereas a linear correlation is the desired result between both different formalisms, the reader should be aware that the methods for calculating the absolute value are different in each formalism. Indeed, (45) is the absolute value of a vector, while (44) is the Kerr angular momentum formula obtained by matching the numerical evolution with a Kerr metric and its associated parameters.

V. FINAL COMMENTS AND CONCLUSIONS

We have numerically calculated the time evolution for the center of mass and intrinsic angular momentum for the 777 cases of black hole coalescing binaries available in the Rochester repository. Since the final outcome of the process is a single black hole, the behavior of R^i and S^j directly gives the position and spin of the final black hole.

To perform the numerical evolution we first derived a one-to-one correspondence between the spin weighted spherical harmonics of the gravitational radiation at the repository and the tensorial harmonics that are present in the equations of motion for R^i and S^j.

We then addressed the issue of the unwanted traveling waves that are present in any initial data and removed them from the equations of motion for the 777 cases. This is done by first finding the relaxation time where the traveling wave is no longer present (amplitude smaller than the numerical error in the calculations). We then obtain the velocity of the center of mass at that time and perform a boost to a new Bondi frame whose origin coincides with the center of mass and is initially at rest. For small traveling waves this translates into a time translation resetting the initial time to the relaxation time.

Using the equations of motion for the global variables available for asymptotically flat spacetimes we numerically obtain the time evolution for D, J, M, and P, and then use these variables to compute R and S.

The outcomes have been divided into two classes for the masses, EM or NEM, and three subclasses for the spins: NS, spinning but aligned with the initial orbital angular momentum, and nonaligned spins.

Some interesting cases are obtained and discussed. In particular, the subclass P of precessing cases exhibit a wide range of different outcomes for the final velocities whereas the NS and A subclasses do not. These appears to be related to the chaotic behavior of the P subclass although a more thorough study is in order. Likewise, the tilting angles of the P subclass have a nonergodic distribution reaching up to 50. This could also be attributed to the chaotic behavior of spinning black holes [22–24]. The F_R is defined and obtained for the 777 cases. Although none of the resulting black holes here analyzed have relativistic speeds, one could easily give a relativistic definition by simply adding a gamma factor to the equation. A quantitative description of the trajectories is also given for representative members of each subclass.

Finally, the change in the Bondi mass and angular momentum are compared between our approach and those from the Rochester catalog. By doing so we single out the gravitational radiation contribution and thus introduce less potential sources of errors. The graphics show a clear correlation between the two approaches with a slope of 1.2 in both graphs. We leave for future work to understand the source of this 20% departure from the ideal correlation.

[1] R. Geroch and J. Winicour, Linkages in general relativity, J. Math. Phys. (N.Y.) **22**, 803 (1981).

[2] O. M. Moreschi, Intrinsic angular momentum and centre of mass in general relativity, Classical Quant. Grav. **21**, 5409 (2004).

[3] L. B. Szabados, Quasi-local energy-momentum and angular momentum in general relativity, Living Rev. Relativity **12**, 4 (2009).

[4] É. É. Flanagan and D. A. Nichols, Conserved charges of the extended bondi-metzner-sachs algebra, Phys. Rev. D **95**, 044002 (2017).

[5] A. D. Helfer, Angular momentum of isolated systems, Gen. Relativ. Gravit. **39**, 2125 (2007).

[6] T. M. Adamo, E. T. Newman, and C. Kozameh, Null geodesic congruences, asymptotically-flat spacetimes and their physical interpretation, Living Rev. Relativity **15**, 1 (2012).

[7] C. N. Kozameh and G. D. Quiroga, Center of mass and spin for isolated sources of gravitational radiation, Phys. Rev. D **93**, 064050 (2016).

[8] C. Kozameh, J. Nieva, and G. Quiroga, Relativistic center of mass in general relativity, Phys. Rev. D **101**, 024028 (2020).

[9] J. Healy and C. O. Lousto, Third RIT binary black hole simulations catalog, Phys. Rev. D **102**, 104018 (2020).

[10] E. Newman and K. Tod, Asymptotically flat space-times, in *General Relativity and Gravitation*, edited by A. Held (Plenum Press, New York, 1980), Vol. 2.

[11] J. N. Goldberg, A. J. MacFarlane, E. T. Newman, F. Rohrlich, and E. G. Sudarshan, Spin-s spherical harmonics and eth, J. Math. Phys. (N.Y.) **8**, 2155 (1967).

[12] C. N. Kozameh, J. I. Nieva, and G. D. Quiroga, Spin and center of mass comparison between the post-newtonian approach and the asymptotic formulation, Phys. Rev. D **98**, 064005 (2018).

[13] E. T. Newman and G. Silva-Ortigoza, Tensorial spin-s harmonics, Classical Quant. Grav. **23**, 497 (2006).

[14] J. Winicour, Angular momentum in general relativity, in *General relativity and gravitation*, edited by A. Held (Plenum Press, New York, 1980), Vol. 2.

[15] H. Nakano, J. Healy, C. O. Lousto, and Y. Zlochower, Perturbative extraction of gravitational waveforms generated with Numerical Relativity, Phys. Rev. D **91**, 104022 (2015).

[16] J. Healy, C. O. Lousto, and Y. Zlochower, Remnant mass, spin, and recoil from spin aligned black-hole binaries, Phys. Rev. D **D90**, 104004 (2014).

[17] P. Mandrilli, J. Nieva, and G. Quiroga, Correspondence between tensorial spin-s and spin-weighted spherical harmonics, Gen. Relativ. Gravit. **52**, 58 (2020).

[18] R. Numerical Realtivity Group, Catalog of numerical simulations, https://ccrg.rit.edu/numerical-simulations.

[19] E. Berti, V. Cardoso, J. A. Gonzalez, U. Sperhake, M. Hannam, S. Husa, and B. Brügmann, Inspiral, merger, and ringdown of unequal mass black hole binaries: A multipolar analysis, Phys. Rev. D **76**, 064034 (2007).

[20] C. Reisswig and D. Pollney, Notes on the integration of numerical relativity waveforms, Classical Quant. Grav. **28**, 195015 (2011).

[21] C. Reisswig, pyGWanalysis, https://svn.einsteintoolkit.org/pyGWAnalysis/trunk/.

[22] C. Kozameh and G. Quiroga, Spin stability of a binary black hole coalescence, Phys. Rev. D **102**, 064015 (2020).

[23] X. Wu and G. Huang, Ruling out chaos in comparable mass compact binary systems with one body spinning, Mon. Not. R. Astron. Soc. **452**, 3167 (2015).

[24] J. Levin, Chaos and order in models of black hole pairs, Phys. Rev. D **74**, 124027 (2006).